Comparison between Backscatter Lidar and Radiosonde Measurements of the Diurnal and Nocturnal Stratification in the Lower Troposphere

GIOVANNI MARTUCCI, RENAUD MATTHEY, AND VALENTIN MITEV

Observatory of Neuchâtel, Neuchâtel, Switzerland

HANS RICHNER

Institute for Atmospheric and Climate Science, ETH Zurich, Switzerland

(Manuscript received 10 March 2006, in final form 8 August 2006)

ABSTRACT

A collection of boundary layer heights has been derived from measurements performed by a ground-based backscatter lidar in Neuchâtel, Switzerland (47.000°N, 6.967°E, 485 m ASL). A dataset of 98 cases have been collected during 2 yr. From these data, 61 are noon and 37 are midnight cases. The following two different schemes were used to retrieve the mixed layer depth and the height of the residual layer from the measurements: the gradient and variance methods. The obtained values were compared with those derived from the potential temperature profiles as computed from radiosonde data. For nocturnal cases, the height of the first aerosol layer above the residual layer was also compared to the corresponding potential temperature value. Correlation coefficients between lidar and radiosonde in both convective and stable conditions are between 0.88 and 0.97.

1. Introduction

The mixed layer depth (MLD; see the appendix for a list of acronym and symbol definitions) and the height of the residual layer (RL) top are two important parameters characterizing the aerosol stratification in the atmospheric boundary layer (ABL) (Stull 1988; McIlveen 1992; Siebert et al. 2001). Several studies focused on the dynamics of nighttime and daytime ABL and aimed to forecast its temporal evolution (De Wekker et al. 1997; Rampanelli and Zardi 2004; Zampieri et al. 2005). The approximation of the current boundary layer height (both day and night) is usually retrieved from the temperature inversion at the top of the ABL as measured by radiosondes, or from the gradient in the water vapor mixing ratio (Heffter 1980; Stull 1988). One convenient and widely used method for the daytime determination of MLD by radiosonde measurements (Cramer 1972; Van Pul et al. 1994; De Wekker et al. 2004) is based on the local maxima of the potential temperature vertical gradient.

Corresponding author address: Valentin Mitev, Observatory of Neuchâtel, Rue de l'Observatoire 58, Neuchâtel CH-2000, Switzerland.
E-mail: valentin.mitev@ne.ch

DOI: 10.1175/JTECH2036.1

The elastic backscatter lidar signal is determined by the altitude profile of the atmospheric aerosol. By using an aerosol as a tracer for convective and mixing processes, the backscatter signal provides information on the ABL stratification. As a remote sensing instrument, the lidar has advantages in detecting the MLD and RL height, in particular, in the possibility to perform continuous measurements and to choose the direction of probing.

The lidar signal gradient gives information about the structure of the ABL, as demonstrated by Russell et al. (1974). This method is widely used and examples thereof may be found in recent studies like those of Menut et al. (1999), Bösenberg and Linné (2002), Frioud et al. (2003, 2004), and Matthias et al. (2004). The results from different approaches to the lidar signal derivative methods for MLD determination have been compared in Sicard et al. (2006). The study was performed for daytime measurements only where it also included correlation with the MLD determined from radiosonde temperature profiles. In another recent study (Wiegner et al. 2006), the authors compare the lidar signal derivative method with results from sodar, radiosoundings, and in situ aerosol measurement of the vertical profile of the aerosol distribution.

The measurements are again performed during daytime.

Hooper and Eloranta (1986) and Piironen and Eloranta (1995) evaluated the MLD with another method, the standard deviation of backscatter signal. The method was further developed by Menut et al. (1999) and referred as a centroid method; therein, the altitude of the maximum of lidar signal variance over a period of 5 min was considered as an estimation of the MLD. The authors compared the MLD obtained with such a procedure and the MLD determined from the Richardson number, where the latter was retrieved from radiosonde measurements. They considered four daytime convective cases and found good agreement between both methods. Another approach to evaluate the current boundary layer height directly from the lidar signal is based on the determination of the altitude where the backscatter signal drops below a defined threshold (Melfi et al. 1985). A technique to determine the altitude of this drop, based on the wavelet technique, was suggested and used in a number of studies (Hayden et al. 1997; Steyn et al. 1998, 1999; Hoff et al. 1997; Hägeli et al. 2000). This method has been further developed in Cohn and Angevine (2000), Davis et al. (2000), and Brooks (2003), with the aim to obtain algorithms that allow automated data processing. The wavelet approach became very convenient also for lidar study of the ABL above complex terrain (Blumen 1990), where the multiple layering of the aerosol is a typical situation in both day- and nighttime.

The objective of the present study is to compare two lidar methods with one based on the potential temperature gradient to determine the ABL stratification during day and night. The two lidar methods are based, respectively, on lidar signal gradient and variance. In the previous studies the comparison between lidar and radiosonde methods to determine the MLD was mainly performed in convective conditions and on few cases; there is hardly any systematic comparison between radiosonde and lidar methods to determine RL height in stable nighttime ABL.

The presented comparison includes 98 cases—61 of which are at noon and 37 of which are at midnight. All cases coincide in time with radiosoundings from a nearby aerological station. The cases from data collection were selected for cloud- (cumulus, stratus, altostratus) and fog-free conditions; however, cirrus might be present. No other criteria of selection have been applied, like season or synoptic pressure conditions. All of the nocturnal cases presented at least one elevated aerosol layer above the RL top. This structure is typical for the city of Neuchâtel, Switzerland, which has a complex topography that strongly contributes to the formation of several nocturnal aerosol layers.

2. Boundary layer dynamics and local circulation

Knowledge of the potential temperature lapse rate is usually sufficient to determine the static stability of an atmospheric layer and to identify its boundaries. An inversion corresponds to a sharp increase in local lapse rate of the potential temperature (θ) and respectively to an increase in the static stability (Stull 1988) of the inversion layer. Starting from the ground level, the first maximum of $\partial\theta/\partial h$ (where h is the altitude) is considered as reference height for the actual boundary layer top.

The lidar measurements were performed in Neuchâtel (47.000°N, 6.967°E; 485 m ASL). The city is situated at the foot of the south slope of the Jura mountain range (oriented NE–SW, with the highest elevation at 1609 m ASL), at the side of Lake Neuchâtel (38.3 km long and 8 km wide, oriented in the mountain range direction). In such topographic conditions, it may be expected that the local circulation contributes to the ABL development (Stull 1988; McIlveen 1992) during both day and night.

During daytime, convection may drive anabatic wind (Blumen 1990; McIlveen 1992) along the Jura slope. The anabatic wind normally enhances the mixing process inside the mixed layer (ML). In some cases, when the ML above Neuchâtel is shallow, the anabatic wind may flow over the ML. The outflow results then in an aerosol layer above the Neuchâtel ML. In addition, when the wind is from the W and NW, aerosol layers are advected from the Jura top in the free troposphere (FT) above the Neuchâtel ML. Because these layers appear above the ML, they do not affect the retrieval of the MLD from the lidar signal.

During nighttime, most of the aerosol sediment is in the SBL, but particles remaining from daytime ML are still present in the RL. The constituents can mix at the RL top with advected aerosol layers when they are lying immediately above the RL, diluting its aerosol content. One process of mixing inside the SBL and RL is due to surface winds. The lake and the mountain slope initiate breeze circulation and katabatic flow (Blumen 1990; McIlveen 1992). The combined flows mix with the already established air masses, and hence modify the SBL stratification (Wallace and Hobbs 1977). The two local winds advect air from the Jura slope with an aerosol content that is different from the one in the SBL. When the winds are strong, the turbulent mixing also may affect the RL. As well, the atmosphere above the RL is influenced by the local topography, as it is in the

daytime. The northwesterly wind blowing over Neuchâtel may advect aerosol layers coming from the Jura range and produce several peaks above the RL top in the lidar signal profiles. These peaks are referred further as nocturnal aerosol layers (NALs).

3. Lidar instrument and signal processing

Lidar measurements were performed from May 2000 until February 2003. During this period the lidar was deployed in the frame of the European Commission (EC) project EARLINET (Bösenberg et al. 2002; Bösenberg and Matthias 2003). For this study, the instrument operated with the second harmonic (532 nm) of a Q-switched Nd:YAG laser. The emitted output pulse energy is from 30 to 45 mJ at a pulse repetition rate of 20 Hz. The receiver has a diameter of 25 cm. Altitudes where the field of view (FOV) of the telescope completely overlaps the laser beam section are around 450 m. Photomultipliers and a digital oscilloscope are used for data acquisition in analog mode. Altitude and temporal resolutions of a single lidar profile are 6 m and 60 s, respectively. The temporal resolution $\Delta t = 60$ s comes from the selected acquisition system mode (1000 shots at 20 Hz), plus the transfer time of the accumulated signal (10 s). Part of the transmitted laser power is deviated to a power monitor and is used to normalize the detected atmospheric signal.

The power of the signal $P(h)$, backscattered by an atmospheric layer of thickness (range gate) Dh centered at altitude h, is expressed by the lidar equation (Wandinger 2005) as

$$P(h) = P_L K O(h) \frac{A}{h^2} \Delta h \beta(h) T^2(h) + N, \qquad (1)$$

$$\text{where} \quad T(h) = \exp\left[-\int_0^h \alpha(h')\, dh' \right].$$

Here P_L is the emitted optical power, K the overall optical efficiency of the instrument, A the telescope area, and $T(h)$ the round-trip transmission factor. The last term N is the sum of the electronic and optical background noise. The parameters a and b represent the total extinction and the total backscatter coefficients, respectively. They can be expressed as sum of the molecular and aerosol components:

$$\alpha(h) = \alpha_{\text{aer}}(h) + \alpha_{\text{mol}}(h) \quad \text{and}$$
$$\beta(h) = \beta_{aer}(h) + \beta_{mol}(h). \qquad (2)$$

In the signal processing, the range-corrected signal (RCS) is computed as

$$\text{RCS}(h) = [P(h) - N]h^2. \qquad (3)$$

Before further processing to retrieve the MLD, RL, and NAL heights, the RCS is averaged in altitude to decrease the shot noise component. The new altitude gates (bins) combine a given number of the original 6-m bins. This number increases quadratically with altitudes; the range resolution Δh becomes 60 m at 1 km and 180 m at 4 km. The altitude averaging process leads to a decrease of the range resolution with the altitude, but the shot noise component is maintained almost constant. Further on in this study only altitudes above the laser-telescope full intersection are considered, for these altitudes we assume also that $O(h) \equiv 1$.

a. Gradient method

The gradient of the logarithm of the signal (Bösenberg and Linné 2002) GS allows the extinction coefficient at level h in linear form to be extracted:

$$\text{GS}_i(h) = \frac{d}{dh} \log(\text{RCS}_i) = \frac{d}{dh} \log[\beta_i(h)] - 2\alpha_i(h). \qquad (4)$$

For noon and midnight, i goes from 1 to 60, corresponding to 1 h of measurement. Single GS_i profiles are computed by Eq. (4) using single RCS_i profiles integrated over 60 s and after altitude quadratic binning. The value of GS_i is around zero at altitudes where the aerosol backscatter is approximately constant, like in the ML and FT. The gradient shows local peaks when passing from a layer with high aerosol content to one with low aerosol content (negative peak), or vice versa (positive peak).

During daytime, in the ML, the level of the aerosol content remains almost constant with the altitude up to the height of the first temperature inversion that marks also the transition from the ABL to the FT. Around this height, the aerosol concentration abruptly decreases and the backscattered signal drops accordingly, showing a local minimum in GS_i value.

During nighttime, the first temperature inversion layer above the SBL (capping inversion) corresponds to the top of the RL. The fall speed of particles with diameter $d \leq 1$ μm is on the order of 0.03 cm s^{-1} and less (Salby 1996). Aerosol particles with this diameter and below remain suspended in the residual layer during the night. Because the lidar backscatter signal at the wavelength of 532 nm is more sensitive to particles with the smaller diameters, the RCS_i have quite homogeneous altitude distribution in the RL and a sharp decrease around its top. Corresponding to this altitude, GS_i profiles show local minima to be expected within the inversion layer, capping the RL.

The final GS profile, used in the comparison pre-

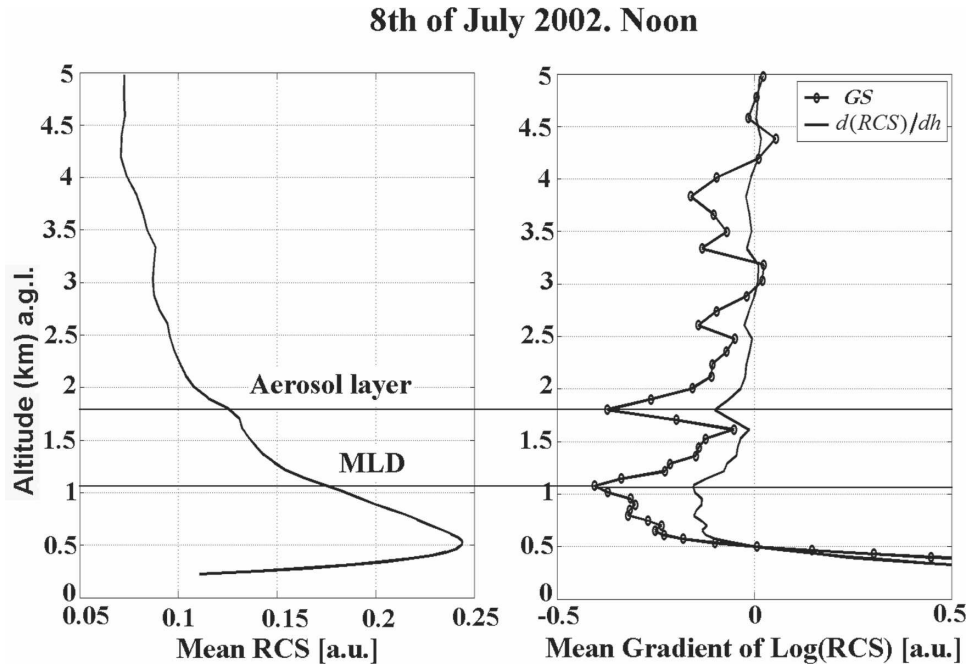

FIG. 1. Mean profiles, averaged over 1 h around noon: (left) mean RCS, and (right) mean GS (heavy solid line) and the mean gradient of the signal (light solid line). Horizontal lines intersect the *y* axis at the height of the MLD and the first aerosol layer above it.

sented below, is obtained as an arithmetic average of the GS_i profiles, measured during 60 min, starting 30 min before noon or midnight. The height corresponding to the minimum value of the mean GS profile $h_{GS_{min}}$ is the height of the aerosol concentration drop defining the averaged boundary layer top during the period of measurement.

The use of $d/dh\{\log[RCS(h)]\}$ [Eq. (4)] for the determination of $h_{GS_{min}}$ is advantageous compared to the use of $d/dh[RCS(h)]$. An advantage is to have the extinction coefficient in linear form, which allows the maxima and minima to appear with better expressed contrast. The two different types of derivatives are compared in Fig. 1. The small value of the signal fluctuation allows minimization of the uncertainty in discriminating false signal gradients produced by the shot noise component from the ones produced by real atmospheric features.

b. Variance method

The variance of RCS is defined as (Menut et al. 1999)

$$\mathrm{Var}(h)_i = \frac{1}{N}\sum_{k=i+1-N/2}^{k=i+N/2}[\mathrm{RCS}_k(h) - \overline{\mathrm{RCS}(h)_i}]^2. \quad (5)$$

For a period of 60 min, the external *i* index goes from 5 to 55. The length of the *k* index is equal to *N*, here with a value of $N = 10$. The internal *k* index of summation represents the individual measurements $k = i - 4, \ldots, i + 5$ in the *N* interval. The mean value $\overline{\mathrm{RCS}(h)_i}$ is obtained by averaging the single RCS_k profiles over *N*. The variance indicates how much the backscatter signal at a fixed *h* varies in respect to $\overline{\mathrm{RCS}(h)_i}$ during the *N* interval. Equation (5) applies to all *i* profiles; passing from profile *i* to profile $i + 1$, the *N* interval shifts by 1 min and makes reference to $\overline{\mathrm{RCS}(h)}_{i+1}$.

In daytime convective conditions, ascending air parcels (updrafts) are thermals arising above the ground and developing inside the ML; descending air parcels (downdrafts) are produced by thermal breakdown at the top of the ML, entraining air from the FT. Figure 2a illustrates the up- and downdraft dynamics around the top of the ML in a convective situation with a typical noon MLD at 1 km. When the convection is moderate, the *free convection scaling velocity* w_*, that is, a velocity scale for the convective boundary layer, can be on the order of $w_* \approx 1.5$–$3.5\ \mathrm{m\ s^{-1}}$. The entrainment zone (EZ) thickness may amount to 300–400 m for an MLD at about 1 km (Flamant et al. 1997; Hägeli 1998). Thermals entering and passing through the EZ will then require about 5–12 min (Stull 1988, p. 463) to reach the top of the ML. In a mean zonal flow of a few meters per second, there will be a diagonal shift of the ascending and descending air parcels. Passing through the FOV of the lidar telescope at different instants, they will cause

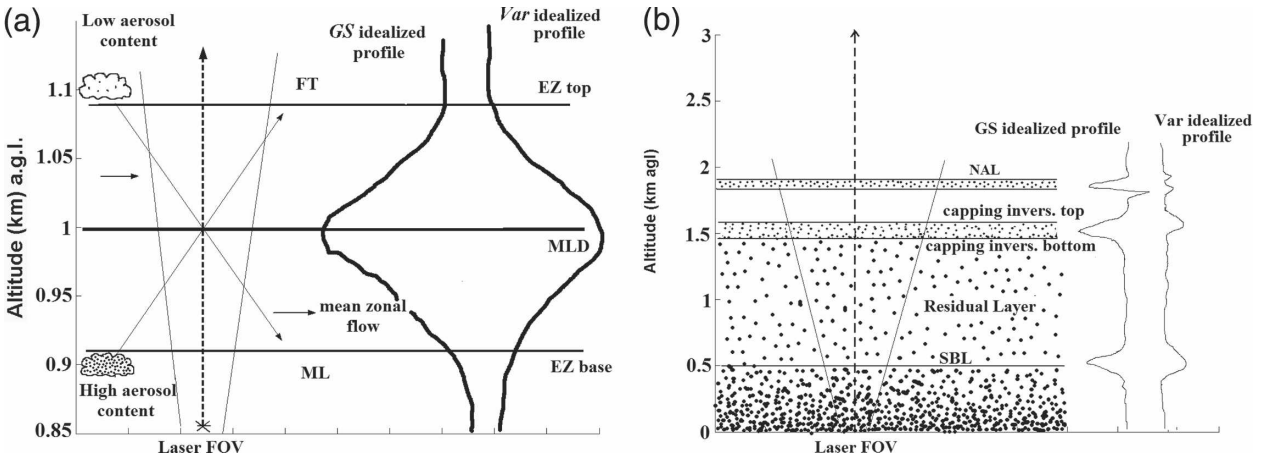

FIG. 2. (a) Simplified presentation of the up- and downdraft dynamics at MLD level. The dashed heavy line is the upward laser beam; empty and filled clouds on the left are the air parcels undergoing updrafts and downdrafts through the EZ, and slanted light lines show the laser FOV. Diagonal shifting is caused by the mean horizontal wind. Idealized GS and Var vertical profiles show minimum and maximum values, respectively, at MLD level. (b) Outline of the aerosol stratification in the nocturnal lower troposphere (SBL, RL, and NAL). Larger aerosols sediment to the bottom of the SBL. Only smaller aerosols stay at higher levels during the whole night as in the capping inversion at the RL top and at the level of NAL, above the RL. Slanted light lines delimit the laser FOV. The upward heavy dashed line shows the laser beam propagation direction. On the right side, the idealized GS and Var profiles are reproduced. Notice that Var has two local maxima: one at the top and one at the bottom of NAL.

variability in the backscattered signal. Applying these considerations to the variance method, we have determined the value of $N = 10$ in Eq. (5), that is, a subinterval duration of 10 min. In this way each single Var_i profile likely covers at least one up-/downdraft event. In cloud-free conditions the buoyancy flux at the surface fuels the thermals at an almost constant rate, keeping the up- and downdraft process active. It is then useful to use a *moving variance* to capture all up- and downdraft events during the period of measurement. Because the top of the ML corresponds to the level at which the mixing of air parcels between the ML and FT is most probable, the Var_i maxima are expected to match the ML top. Thermals may engender large signal variability not only as part of the up- and downdraft process, but also in producing gravitational distortion of the inversion layer with the similar time period as above. The final Var profile is obtained as the arithmetic average of the single Var_i profiles.

In convective conditions, the zone where the aerosol concentration drops and the zone where the exchange with the FT takes place coincide. For this reason we may expect that the altitudes of local minimum in GS and local maximum in Var will be inside this zone (see Fig. 2a).

During nighttime stable conditions, distortions of the inversion layer resulting from gravity waves may lead to backscatter signal variability at that altitude. At the level of the boundary between RL and FT the turbulent mixing resulting from wind shear also generates time variation of the lidar signal. Even when the wind shear is weak or absent, there is nevertheless a mixing between RL and FT; in this case it is significantly lower than in the daytime convective conditions and determines a smaller Var peak. Above the RL top, at the level of the first NAL, the wind profile may show a gradient at both of NAL's boundaries. In such a case, the turbulent mixing take place at both boundaries, producing a double maximum in Var. The vertical distance between the two maxima provides an evaluation of the thickness of the temperature inversion corresponding to NAL (see Fig. 2b).

Following Taylor's hypothesis, a measurement at one point in space over a long time period can be interpreted as an observation of a large region of space at an instant in time. This is possible when the *frozen turbulence* condition is accomplished ($\sigma_w < 0.5W$, where W is the horizontal wind magnitude and σ_w is the standard deviation of the wind speed). This condition is achieved for the already treated idealized case of constant zonal flow of a few meters per second. The 1-h time-averaged Var can be considered a space-averaged profile. The signal variance at the height of temperature inversion will likely show a local maximum representing a measure of the current boundary layer height. After these considerations, the Var maximum at the level of the inversion layer is likely due to both the combined action of the distorting plumes and air parcel mixing in daytime cases and of gravity waves and wind shear during nighttime.

c. Comparison algorithm

The automated procedure we developed first determines the MLD, RL, and NAL heights from the lidar data and, separately, the altitudes of temperature inversions from $\partial\theta/\partial h$. It then correlates the lidar- to the radiosondes-computed values. For lidar-derived heights, no assumptions about the aerosol stratification are needed.

The steps of the automatic lidar data processing start from the measured lidar raw signals with 60-s temporal and 6-m altitude resolutions; the signals are corrected for the electronic noise, laser power variations, optical background, and range (altitude). The initial vertical resolution in the corrected signal is decreased by the quadratic altitude binning between 0 and 8 km AGL to reduce the fluctuations resulting from the signal shot noise component at farther ranges. Single GS_i profiles and the averaged GS are obtained as described in section 3a [see Eq. (4)], with a final averaging time of 60 min. Single Var_i profiles and the averaged Var are obtained as described in section 3b [see Eq. (5)], with a final averaging time of 60 min. The heights of the first (starting from the ground level) minimum and maximum of the GS and Var profiles, respectively, are detected by the algorithm, and the mean value between the two heights is kept as reference height (h_{ref}) for the next steps. The θ profile and its gradient $\partial\theta/\partial h$ are computed from the radiosonde data. A vertical window centered in h_{ref}, and an extension equal to $0.15h_{\text{ref}}$ limits the vertical region in which to search for the principal maximum of $\partial\theta/\partial h$ (e.g., for $h_{\text{ref}} = 1$ km, the window extension is 150 m, from 0.925 to 1.075 km). The three altitudes obtained from GS, Var, and $\partial\theta/\partial h$ each represent an estimation of MLD, RL, or NAL height.

4. Observations

Each case of the elaborated comparison database consists of a lidar measurement over 60 min around noon and midnight, that is, from 1130 to 1230 and from 2330 to 0030 UTC, respectively. Each measurement comprises 60 single profiles of 1-min integration time each. Radiosoundings were performed at the Meteosuisse aerological station in Payerne, approximately 20 km south of Neuchâtel. Radiosonde data contain wind, pressure, temperature, relative humidity, and dewpoint.

The potential temperature θ is retrieved from temperature and pressure as measured by radiosoundings using *Poisson's equation* (Stull 1988). Potential temperature θ and its vertical gradient $\partial\theta/\partial h$ provide the heights of the temperature inversions. These altitudes are then correlated with the MLD, RL, and NAL heights as obtained from the GS and Var methods. Vertical resolution of θ is not constant and depends on the vertical velocity of the sounding balloon; however, θ vertical resolution is always higher than that of Var and GS in the studied range of altitudes (from 0 to 5 km AGL).

a. Noon and midnight lower troposphere: Two examples

Two cases are shown (in Figs. 3 and 5) of measurements taken, respectively, at noon 20 May 2002, and at midnight 13 August 2001. They are presented as examples to illustrate the considerations given in section 3c for the comparison algorithm.

The height of the inversion layer as detected by $\partial\theta/\partial h$ and the MLD retrieved from the two lidar methods are depicted in Fig. 3. The center of the average time interval for mean GS and Var profiles corresponds to noon, when the radiosonde measurement is carried out. The black horizontal line intersects the y axis at the MLD level (i.e., at 1.215 km AGL), computed by the GS method (MLD computed by the Var method is slightly lower, at 1.146 km AGL). Black circles highlight the temperature inversions and the corresponding positive peak in $\partial\theta/\partial h$. The height computed by GS appears in the plot at about 100 m above the top of the temperature inversion layer and about 200 m above the local maximum of $\partial\theta/\partial h$, corresponding to the center of the inversion layer. The aerosol-rich air mass is confined below the first temperature inversion. Therefore, the main decrease in the signal amplitude appears immediately above the inversion level. Consequently, the computed GS minimum is just above the top of the inversion layer. The Var maximum height is principally determined by its *mixing* component; it is not influenced by the contribution from the gravitational distortion of the inversion layer. Because we work with the mean Var profile, the altitude fluctuations of the inversion layer during the time of measurement do not affect its mean position, but make it more spread. Thus, the Var maximum corresponds to the level where most of the exchange process takes place, namely, at or immediately below the inversion layer top.

In Fig. 4 is shown the temporal development of the RCS in the form of a two-dimensional plot corresponding to the case of 20 May 2002. Superimposed to the RCS time series are the values of MLD as computed by single GS_i (white solid line) and Var_i (white dashed line) profiles during the period of lidar observation. The vertical axis extents up to 3 km AGL, not to 5 km, to highlight the atmospheric portion in which the MLD evolves over time.

A summer midnight case, 13 August 2001, is pre-

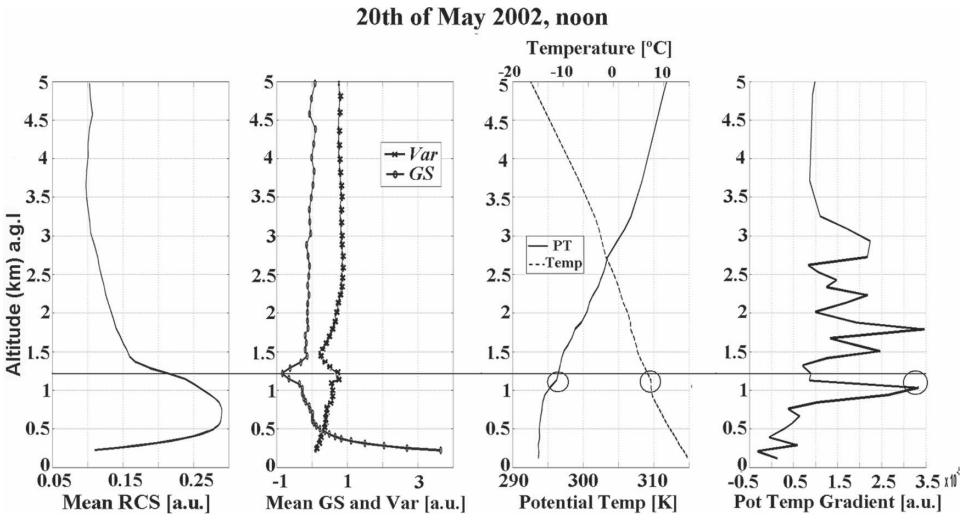

FIG. 3. (left to right) The vertical profiles of mean RCS, mean GS and Var, temperature and θ, and $\partial\theta/\partial h$ are shown. Mean GS and Var vertical profiles are averaged over 1 h. Altitude: km AGL; Payerne is at 491 m ASL and Neuchâtel at 485 m ASL, y axes are shifted for the 6-m difference. The black horizontal line intersects the y axis at the MLD level computed by the GS method. Circles show the temperature inversions and the corresponding positive peak in $\partial\theta/\partial h$.

sented in Fig. 5. The gradient $\partial\theta/\partial h$ in the fourth panel shows several local maxima, indicating a complex nocturnal ABL. Despite this multilayer structure, the heights of GS minima coincide with those of the $\partial\theta/\partial h$ maxima. Horizontal lines in the figure show the heights of the SBL top, RL, and NAL, as computed by the GS. The presence of nocturnal multiple aerosol layers above the RL represents a difficulty when retrieving

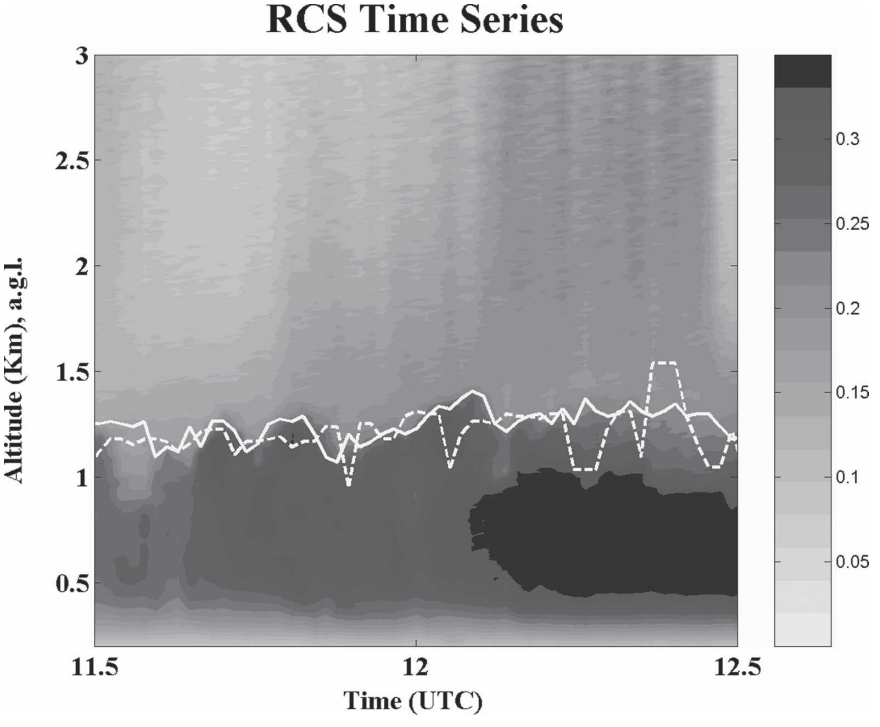

FIG. 4. First 3 km AGL of RCS time–altitude cross section during the 1-h lidar measurement (from 1130 to 1230 UTC) on 20 May 2002. White solid and dashed lines represent the MLD temporal evolutions as computed, respectively, by single GS_i and Var_i profiles. Vertical and temporal resolutions are, respectively, 12 m and 60 s.

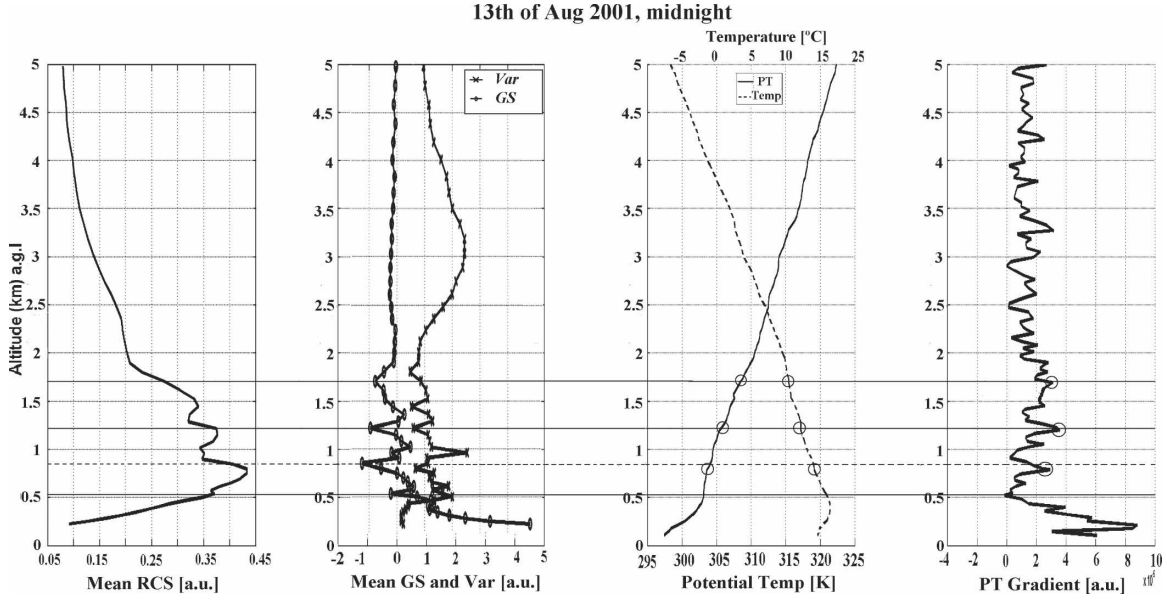

FIG. 5. (left to right) Mean RCS, mean GS and Var, temperature and θ, and $\partial\theta/\partial h$. The first (from ground level) black horizontal line intersects the y axis at the SBL top level. The dashed line intersects the RL top level. The other two solid lines intersect with the y axis at the level of the NALs above the RL top. All the lines pass through the heights computed by the GS method.

the RL top height, in particular when these layers are close to it. The first maximum of $\partial\theta/\partial h$ at about 200 m matches the center of the superadiabatic layer, that is, the SBL. Above this level the first horizontal line intersects the y axis at 537 m AGL at the level of the SBL top. As expected (Stull 1988, p. 17), the top of the SBL does not correspond to any temperature inversion; nevertheless, it is indicated by the decrease in the backscatter signal and, respectively, by the negative peak in GS. Above the SBL, at the RL top, the dashed horizontal line passes through the GS minimum, appearing slightly above the corresponding $\partial\theta/\partial h$ maximum. The two solid horizontal lines above the RL intersect the y axis at 1.215 and 1.707 km, showing the levels of two elevated NALs. In both cases the lines match the corresponding $\partial\theta/\partial h$ maxima. The Var profiles show, at the levels of SBL, RL, and the first NAL, similar structures: one more pronounced maximum at a lower altitude, below the GS minimum, and another, less pronounced peak at a higher altitude, above or at the level of the GS minimum. From the radiosonde data we inspected the vertical profile of wind direction, and found a shear at the inversion boundaries of the RL top and the first NAL. The turbulent mixing at these levels resulting from wind shear determines the two Var peaks. Gradient GS has a minimum inside the inversion layer matching the level of the maximum decrease of aerosol backscatter. The maxima of $\partial\theta/\partial h$ are found approximately at or a little below the level of the GS minimum and are definitely below the higher Var maximum (as illustrated in Fig. 2b).

In Fig. 6, the temporal development of the RCS is in the form of a two-dimensional plot, corresponding to the case of 13 August 2001. Superimposed to the RCS time series are the values of the RL top as computed by single GS_i (white solid line) and Var_i (white dashed line) profiles during the period of lidar observation. The vertical axis extents up to 3 km AGL, not to 5 km, to highlight the atmospheric portion in which the RL top evolves over time.

b. Uncertainty estimation

The combined temporal and altitude averaging reduces the shot noise level. As an example, for a single RCS profile without altitude binning, the shot noise component σ_{shot} at 2 km is 4% of the RCS value. Averaging reduces the shot noise contribution by a factor of $E = (N_p N_b)^{0.5}$, where N_p and N_b are, respectively, the number of profiles and the number of bins used for averaging. Hence, the shot noise after the average process is $\sigma_{\text{Av}} = \sigma_{\text{shot}} \times E^{-1}$. Typically, $N_p = 60$ and $N_b = 17$ at 2 km, so E equals 32. It is noted that the resulting temporal and vertical resolutions after averaging are comparable with those applied in previous lidar studies of MLD (Matthias et al. 2004). In the present analysis, σ_{Av} is reduced to negligible values compared to the uncertainty contributions described below.

Based on calculations and test calibrations (Ruffieux

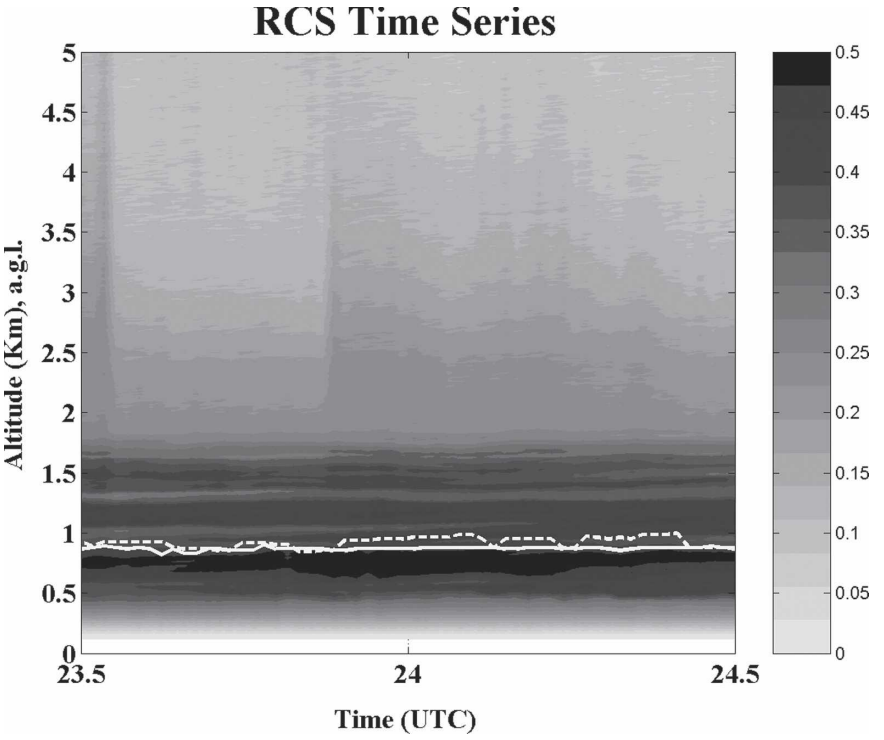

FIG. 6. First 3 km AGL of RCS time–altitude cross section during the 1-h lidar measurement (from 2330 to 0030 UTC) on 13 Aug 2001. White solid and dashed lines represent the RL temporal evolutions as computed, respectively, by single GS_i and Var_i profiles. Vertical and temporal resolutions are, respectively, 12 m and 60 s.

and Joss 2003), the radiosonde-measured values of air temperature are assigned, for the cases selected in this study, with an error σ_T equal to 0.2 K. This means computing θ by the Poisson equation, an error of ± 0.3 K AGL, and an error of ± 0.34 K at 5 km AGL. Taking the larger error (in absolute value) $\sigma_\theta = 0.34$ K, this corresponds to a maximum altitude uncertainty of about $\Delta H_\theta = \pm 60$ m.

Possible uncertainty sources affecting lidar and radiosonde comparisons could be the geographic distance between Neuchâtel and Payerne, the difference in the time duration of the two measurements (on average 1 h for the lidar and several minutes for the radiosonde ascent), and the bias induced by using two different methods, GS and Var.

The area of Payerne is expected to be affected by a similar local circulation as that of the area of Neuchâtel. The aerological station is 20 km south of Neuchâtel on the lake's opposite shore. During night, the lake presence modifies the SBL by engendering breeze circulation in both Neuchâtel and Payerne. When the wind blows from the NW, elevated aerosol layers are advected from the Jura toward Neuchâtel. In a mean northwesterly flow of 10 m s^{-1}, this aerosol layer may be advected from Neuchâtel to Payerne in about 30 min. Following these considerations, we assume that the geographic distance between the two sites does not introduce major uncertainties in this study.

While lidar-computed altitudes result from an average over 1 h, radiosoundings are spot measurements of only a few minutes of duration carried out during the central part of the lidar observation. An estimation of the induced uncertainty is given by the altitude variations of the minimum and the maximum of single GS_i and Var_i profiles, respectively, during lidar measurement. Some representative cases have been taken from the database to compute the differences in altitude between the highest and lowest extremes of both GS_i and Var_i observed during the 1-h interval. For each method (either GS or Var) and for each type of measurement (noon or midnight) a mean value of these differences represents an estimation of the uncertainty; for midnight or noon (subscripts m or n, respectively) this is indicated by the symbol $\xi_{m(n)}$. Because $\xi_{m(n)}$ is computed for each lidar method, we have a total of four uncertainties: $\xi_{m(n),\mathrm{GS(Var)}}$. The four obtained ξ values are as follows: $\xi_{n,\mathrm{GS}} \approx 340$ m, $\xi_{n,\mathrm{Var}} \approx 240$ m, $\xi_{m,\mathrm{GS}} \approx 110$ m, and $\xi_{m,\mathrm{Var}} \approx 90$ m.

The fact that the ξ values are larger for the noon cases shows that during noon measurements the differ-

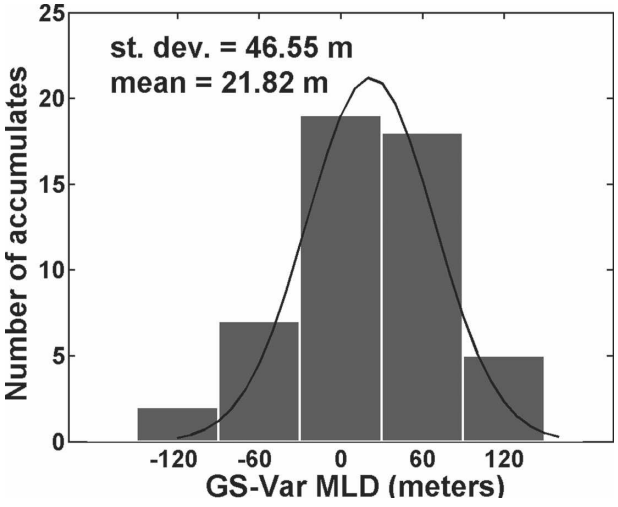

FIG. 7. Histogram of $MLD_{GS} - MLD_{Var}$ noon values; x-axis resolution is 60 m, equal to the GS and Var vertical resolution at 1 km.

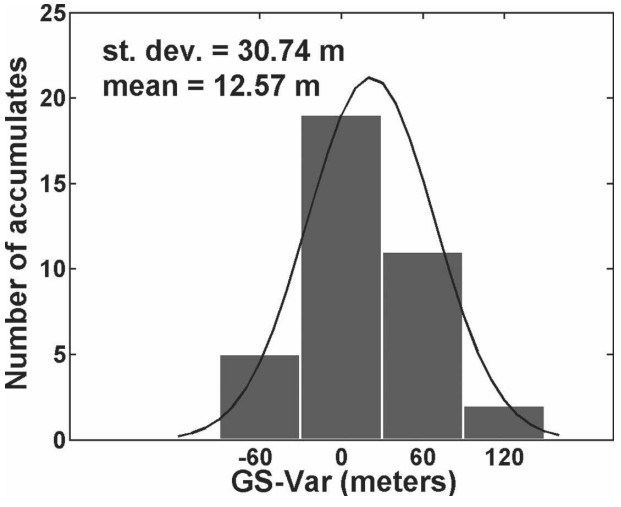

FIG. 8. Histogram of $RL_{GS} - RL_{Var}$ midnight values; x-axis resolution is 60 m, equal to the GS and Var vertical resolution at 1 km.

ence between the lowest and highest observed ML top is larger than that in the midnight cases. At Neuchâtel's latitude, summer is the season in which the ML may reach a maximum depth in the early afternoon, at around 1500 CET (1400 UTC). This means that at noon the ML is still growing. We assume then that the principal reason for determining the large ξ value at noon is due to the contribution of summer cases; that is, during noon measurements we may expect a larger discrepancy between the radiosonde and the lidar.

There is no a priori reason for either one of the two methods to be closer to the "true" value than the other (here the true value is determined by $\partial\theta/\partial h$). In Fig. 7 and Fig. 8, histograms show frequencies of the differences between the altitudes retrieved from GS and Var in noon and midnight cases, respectively. We assume that the differences $MLD_{GS} - MLD_{Var}$ and $RL_{GS} - RL_{Var}$ distribute according to the standard normal density function. The Gaussian $F_{x,\mu,\sigma}$ is superimposed to the histograms, where on the x axis there are the $MLD_{GS} - MLD_{Var}$ and $RL_{GS} - RL_{Var}$ differences; μ and σ are, respectively, the mean value and the standard deviation of the x values. The standard deviation represents the uncertainty in evaluating the MLD and the RL height using either the GS or Var method.

The approximated normal distributions show a mean positive shift for both noon and midnight cases. For noon cases, the mean value μ is 22 m, and the standard deviation σ is 47 m. For midnight cases, μ is 13 m and σ is 31 m. The results show that "zero" is the most frequently obtained value for both the noon and midnight cases; hence, zero is the statistic *mode* of the distributions. The positive values of μ lead to conclusion that the heights computed by the GS method are statistically higher than the heights computed by the Var method. The resulting bias is $b_{m(n)} = \mu \pm \sigma$, where the subscripts m and n have the same meaning as for $\xi_{m(n)}$.

The total uncertainty is then

$$U_{\text{tot}} = b_x \pm \xi_{x,y}/2, \tag{6}$$

where $x = m$ or n (for midnight or noon measurements) and y = GS or Var (depending on the selected lidar method). The values of ξ are used in the correlation plots (Figs. 9a–10b) to express the amplitude of the error bars $\pm\xi_{m,n,\text{GS,Var}}/2$. Error bars also appear on altitudes as retrieved from $\partial\theta/\partial h$ values in Figs. 9a–10b, with amplitudes equal to ± 60 m.

c. *Correlation between lidar methods and potential temperature*

Correlations are shown in Figs. 9a–11b. All data distributions are linearly fitted without forcing the line to pass through the axis origin. The line equations in the plots have the form $y = ax + b$. Correlation coefficients have to be interpreted in respect to the offset b and slope a. Both parameters are due to the combined presence of bias $b_{m(n)}$ and statistical under- and overestimates introduced by the use of GS and Var. An overestimate means that the height computed by GS or Var is higher than the one retrieved from $\partial\theta/\partial h$, and vice versa for an underestimate. Investigation of x and y values for which GS or Var overestimate $\partial\theta/\partial h$ is done by studying the relation $y/x > 1$.

1) *GS* AND Θ

The correlation between MLD_{GS} and MLD_{θ} for the noon cases is illustrated in Fig. 9a. Measurements from

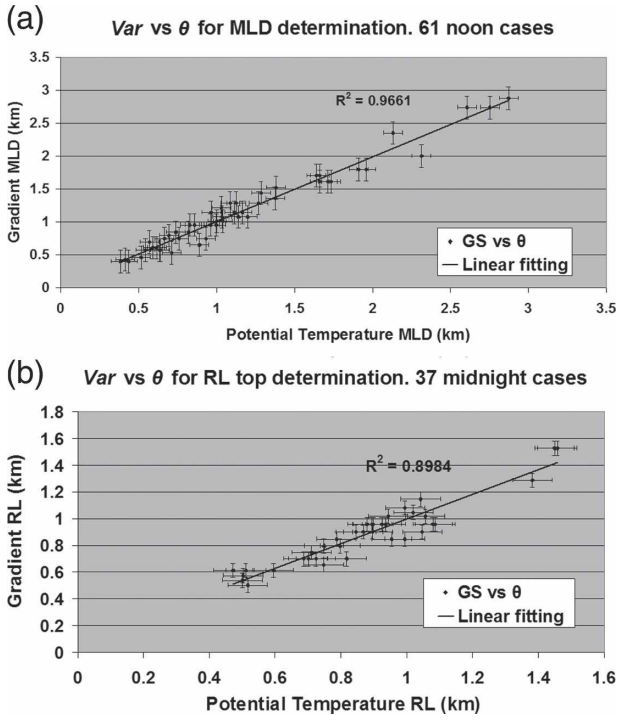

FIG. 9. (a) Correlation between MLD computed by GS and $\partial\theta/\partial h$ for 61 noon cases. Error bar amplitude $\xi_{n,\mathrm{GS}}$ on y values is equal to 340 m; error bars on x values have amplitudes equal to $2\Delta H_\theta = 120$ m; correlation coefficient is 0.96. The slope and the offset of the fit line are 0.98 and 0.028 km, respectively. (b) Correlation between RL computed by GS and $\partial\theta/\partial h$ for 37 midnight cases. Error bar amplitude $\xi_{m,\mathrm{GS}}$ on y values is equal to 110 m; error bars on x values have amplitudes equal to $2\Delta H_\theta = 120$ m; correlation coefficient is 0.92. The slope and the offset of the fit line are 0.944 and 0.063 km, respectively.

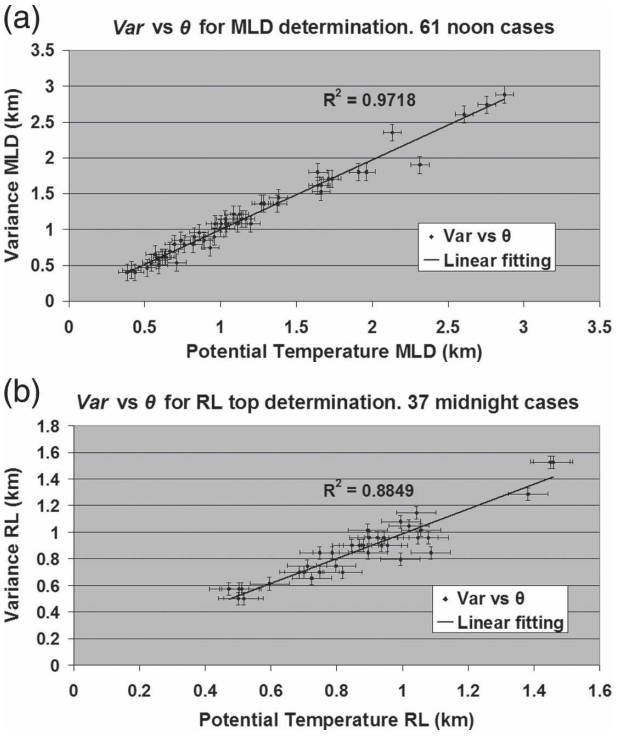

FIG. 10. (a) Correlation between MLD computed by Var and $\partial\theta/\partial h$ for 61 noon cases. Error bar amplitude $\xi_{n,\mathrm{Var}}$ on y values is equal to 240 m; error bars on x values have amplitudes equal to $2\Delta H_\theta = 120$ m; correlation coefficient is 0.90. The slope and the offset of the fit line are 0.924 and 0.073 km, respectively. (b) Correlation between RL computed by Var and $\partial\theta/\partial h$ for 37 midnight cases. Error bars amplitude $\xi_{m,\mathrm{Var}}$ on y values is equal to 90 m; error bars on x values have amplitudes equal to $2\Delta H_\theta = 120$ m; correlation coefficient is 0.88. The slope and the offset of the fit line are 0.932 and 0.057 km, respectively.

the data collection are representative for different seasons as well as for various atmospheric conditions in terms of temperature, humidity, wind, and pressure. Nevertheless, the data points in Fig. 9a are distributed closely around the linear fit with a correlation coefficient $R^2 = 0.96$ (error bars are $\pm\xi_{n,\mathrm{GS}}/2$). This demonstrates that convective MLD obtained from lidar and radiosonde methods are statistically well correlated, independently from the difference in synoptic conditions. Data between 0.5 and 1.5 km distribute fairly homogeneously and represent 75% of the cases. Relative to $\partial\theta/\partial h$, GS provides a statistical overestimate of the MLD for altitudes up to 1.8 km (linear fit: $y = 0.98x + 0.03$).

The correlation between $\mathrm{RL_{GS}}$ and RL_θ for the midnight cases is shown in Fig. 9b. Two-thirds of the data distribute between 0.4 and 1 km. Correlation coefficient R^2 is equal to 0.90; the offset is 73 m and the slope is 0.92, with error bars $\pm\xi_{m,\mathrm{GS}}/2$. From these parameters it is found that GS underestimates the height of the RL top for ranges above 0.96 km. Examining the distribution in the plot, we see that the data are split at about 40% above and 60% below this range.

2) *VAR* AND Θ

Figures 10a and 10b present the correlation between Var and $\partial\theta/\partial h$, respectively, for the noon and midnight cases. Error bars have the same meaning as in Figs. 9a and 9b, but with the different values $\pm\xi_{n,\mathrm{Var}}/2$ in Fig. 10a and $\pm\xi_{m,\mathrm{Var}}/2$ in Fig. 10b. The correlation coefficient R^2 in Fig. 10a equals 0.97, a value slightly higher than for the (GS, $\partial\theta/\partial h$) noon correlation. The nighttime correlation coefficient is again lower than that of the daytime, with a value of $R^2 = 0.88$. In Fig. 10a, Var overestimates the MLD value for altitudes below 1.1 km (40% of the data). In Fig. 10b, the overestimate occurs for altitudes below 0.7 km (30% of the data). In both daytime and nighttime correlation plots, GS estimations of MLD and RL height are statistically higher

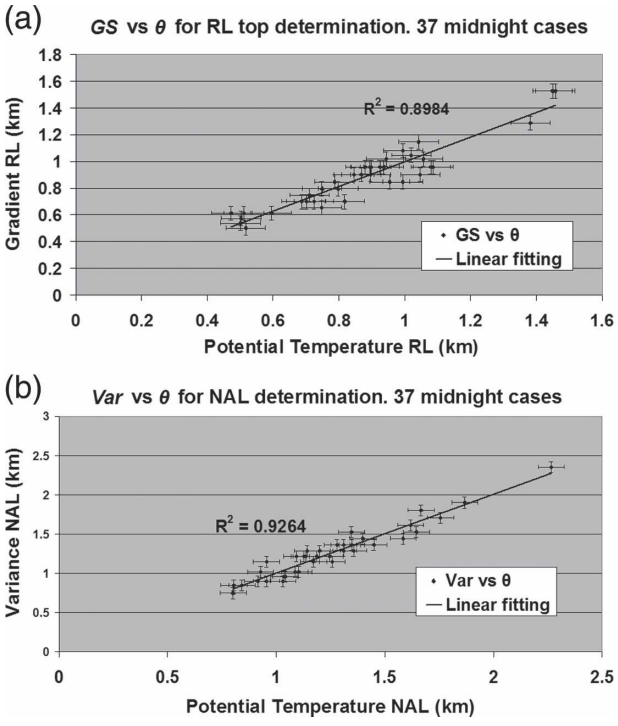

FIG. 11. (a) Correlation between NAL computed by GS and $\partial\theta/\partial h$ for 37 midnight cases. Error bar amplitude $\xi_{m,\mathrm{GS}}$ on y values is equal to 80 m; error bars on x values have amplitudes equal to $2\Delta H_\theta$ = 120 m; correlation coefficient is 0.92. The slope and the offset of the fit line are 0. 944 and 0.063 km, respectively. (b) Correlation between NAL computed by Var and $\partial\theta/\partial h$ for 37 midnight cases. Error bar amplitude $\xi_{m,\mathrm{Var}}$ on y values is equal to 140 m; error bars on x values have amplitudes equal to $2\Delta H_\theta$ = 120 m; correlation coefficient is 0.92. The slope and the offset of the fit line are 1.005 and 0.001 km, respectively.

than those computed by Var for most of the altitude intervals. This is consistent with the positive bias $b_{m,n}$ shown in Figs. 7 and 8.

3) HEIGHT OF NOCTURNAL AEROSOL LAYERS

For the determination of NAL height we select the altitude of the higher Var maximum, that is, the one likely matching the top of the NAL (see Fig. 2b). The uncertainty resulting from the variation of the single NAL heights computed during the 1-h average is indicated by $\xi_{m,\mathrm{GS,Var}}$ and determines the amplitude of the error bars in the correlation plots (see Figs. 11a and 11b). As for the MLD and RL determination, for NAL the values of $\xi_{m,\mathrm{GS}}$ and $\xi_{m,\mathrm{Var}}$ also come from an average of the vertical differences between the highest and the lowest peak of GS_i and Var_i during 1 h for some representative case. The obtained values for $\xi_{m,\mathrm{GS}}$ and $\xi_{m,\mathrm{Var}}$ are 80 and 140 m, respectively. The value of U_{tot} for NAL heights has the same expression as in Eq. (6),

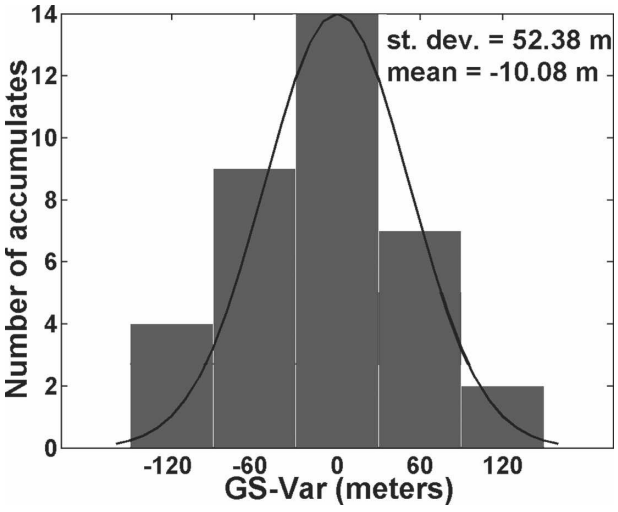

FIG. 12. Histogram of $\mathrm{NAL_{GS}} - \mathrm{NAL_{Var}}$ values; x-axis resolution is 60 m, equal to the GS and Var vertical resolution at 1 km.

where the bias $b_{m,n}$ is replaced by b_m computed from the distribution in Fig. 12.

As shown in Figs. 11a and 11b, NAL heights distribute mainly between 0.8 and 1.8 km. The retrieved correlation coefficients R^2 are comparable—0.925 for (GS, $\partial\theta/\partial h$) and 0.926 for (Var, $\partial\theta/\partial h$). In the altitude interval of 0.8–1.8 km, the linear fit of (GS, $\partial\theta/\partial h$) provides an underestimate of NAL height for altitudes above 1.16 km, that is, in 65% of the cases. In the same altitude interval, Var maxima give an overestimate of the NAL height because it is detected by $\partial\theta/\partial h$, for altitudes above 0.87 km, that is, 80% of the cases. In accordance to this, the mean value of the distribution of differences between $\mathrm{NAL_{GS}}$ and $\mathrm{NAL_{Var}}$ in Fig. 12 is negative. This shows that the levels of Var maxima are statistically higher than the levels of GS minima.

5. Conclusions

This study presents a comparison between backscatter lidar and radiosonde temperature methods for the determination of the ABL stratification. Measurements were performed in different synoptic conditions, but always in the cloud-free low troposphere. The retrieved lidar MLD for daytime and the heights of RL and NAL for nighttime have been compared to the heights of temperature inversion layers detected by radiosounding. A total of 98 cases (61 for daytime, 37 for nighttime) have been statistically evaluated.

For daytime the correlation coefficient R^2 = 0.96 when comparing the lidar gradient method (GS) with the radiosonde potential temperature gradient ($\partial\theta/\partial h$). A similar value (0.97) is obtained when correlating the lidar variance method (Var) with $\partial\theta/\partial h$.

For nocturnal cases the correlation coefficients are slightly lower, $R^2 = 0.90$ for (GS, $\partial\theta/\partial h$) and $R^2 = 0.88$ for (Var, $\partial\theta/\partial h$). The lower values of R^2 during nighttime are due to the aerosol multilayer structure present immediately above the RL top, which makes its height detection more difficult.

The top altitude of NAL detected by the lidar instrument is in good agreement with the θ vertical profiles. The correlation coefficients are $R^2 = 0.92$ for (GS, $\partial\theta/\partial h$) and $R^2 = 0.93$ for (Var, $\partial\theta/\partial h$).

As we see, the correlation between lidar and radiosonde methods in detecting MLD, RL, and NAL heights always has coefficients greater than 0.88 for both day- and nighttime. The combination of the lidar signal gradient and the variance allows for unambiguous identification of the MLD in convective conditions, as well as the aerosol stratification, including RL and NAL heights in nocturnal stable ABL. The evaluation of these altitudes is done by a simple and efficient algorithm that consents automated data processing. This is an advantage when performing continuous long-term lidar measurements of the ABL development. In summary, this study shows that the heights of the ML during daytime, and the RL and NAL during nighttime, can be retrieved directly from backscatter lidar data and may be related to the ABL structure as represented by the temperature profile.

Acknowledgments. This study was funded by Swiss OFES Contract 99.0650-1 as part of the EU project EARLINET and by Swiss National Science Foundation Subsidy 2000-067051.01/1. The authors greatly acknowledge MeteoSwiss, Aerological Station Payerne for the upper-air data.

APPENDIX

List of Acronyms and Symbols

Following is a list of the acronyms and symbols used in text, listed in alphabetic order.

ABL	Atmospheric boundary layer
AGL	Above ground level
ASL	Above sea level
CET	Central European Time
EARLINET	European Aerosol Research Lidar Network
EC	European Commission
EZ	Entrainment zone
FOV	Field of view
FT	Free troposphere
GS	Gradient signal
ML	Mixed layer
MLD	Mixed layer depth
NAL	Nocturnal aerosol layer
NE	Northeast
NW	Northwest
RCS	Range-corrected signal
RL	Residual layer
SBL	Stable boundary layer
SW	Southwest
UTC	Universal coordinated time
Var	Variance
W	West
θ	Potential temperature
σ_θ	Statistical error on potential temperature
ΔH_θ	Total uncertainty on θ-computed heights

REFERENCES

Blumen, W., 1990: *Atmospheric Processes over Complex Terrain. Meteor. Monogr.,* No. 45, Amer. Meteor. Soc., 323 pp.

Bösenberg, J., and H. Linné, 2002: Laser remote sensing of the planetary boundary layer. *Meteor. Z.,* **11,** 233–240.

——, and V. Matthias, 2003: EARLINET: European Aerosol Research Lidar Network to establish an aerosol climatology. MPI Tech. Rep. 348, 191 pp.

——, and Coauthors, 2002: EARLINET: Establishing the European Aerosol Research Lidar Network. Lidar Remote Sensing in Atmospheric and Earth Sciences. *Proc. 21st Int. Laser Radar Conf.,* Quebec City, QC, Canada, Defense R&D Canada, Valcartier, 293–296.

Brooks, I. M., 2003: Finding boundary layer top: Application of a wavelet covariance transform to lidar backscatter profiles. *J. Atmos. Oceanic Technol.,* **20,** 1092–1105.

Cramer, O. P., 1972: Potential temperature analysis for mountainous terrain. *J. Appl. Meteor.,* **11,** 44–50.

Cohn, S. A., and W. M. Angevine, 2000: Boundary layer height and entrainment zone thickness measured by lidars and wind-profiling radars. *J. Appl. Meteor.,* **39,** 1233–1247.

Davis, K. J., N. Gamage, C. R. Hagelberg, C. Kiemle, D. H. Lenschow, and P. P. Sullivan, 2000: An objective method for deriving atmospheric structure from airborne lidar observations. *J. Atmos. Oceanic Technol.,* **17,** 1455–1468.

De Wekker, S. F. J., M. Kossmann, and F. Fielder, 1997: Observations of daytime mixed layer heights over mountainous terrain during the TRACT field campaign. *Proc. 12th Symp. on Boundary Layers and Turbulence,* Vancouver, BC, Canada, Amer. Meteor. Soc., 498–499.

——, D. G. Steyn, and S. Nyeki, 2004: A comparison of aerosol-layer and convective boundary-layer structure over a mountain range during STAAARTE '97. *Bound.-Layer Meteor.,* **113,** 249–271.

Flamant, C., J. Pelon, P. H. Flamant, and P. Durand, 1997: Lidar determination of the entrainment zone thickness at the top of the unstable marine atmospheric boundary layer. *Bound.-Layer Meteor.,* **83,** 247–284.

Frioud, M., V. Mitev, R. Matthey, C. Häberli, H. Richner, R. Werner, and S. Vogt, 2003: Elevated aerosol stratification above Rhine Valley under strong anticyclonic conditions. *Atmos. Environ.,* **37,** 1785–1797.

——, ——, ——, H. Richner, M. Furger, and S. Gubser, 2004: Variation of the aerosol stratification over the Rhine Valley

during Foehn development: A backscatter lidar study. *Meteor. Z.,* **NF13,** 175–181.

Hägeli, P., 1998: Evaluation of a new technique for extracting mixed layer depth and entrainment zone thickness from lidar backscatter profiles. M.S., Dept. of Geography, Swiss Federal Institute of Technology ETHZ, 67 pp.

——, D. G. Steyn, and K. B. Strawbridge, 2000: Spatial and temporal variability of mixed-layer depth and entrainment zone thickness. *Bound.-Layer Meteor.,* **97,** 47–71.

Hayden, K. L., K. G. Anlauf, R. M. Hoff, J. W. Strapp, J. W. Bottenheim, H. A. Wiebe, F. A. Froude, and J. B. Martin, 1997: The vertical chemical and meteorological structure of the boundary layer in the lower Fraser Valley during Pacific '93. *Atmos. Environ.,* **31,** 2089–2105.

Heffter, J. L., 1980: Air Resource Laboratories atmospheric transport and dispersion model. NOAA Tech. Memo. ERL ARL-81, 24 pp.

Hoff, R. M., M. Harwood, A. Sheppard, F. Froude, and J. B. Martin, 1997: Use of airborne lidar to determine aerosol sources and movement in the Lower Fraser Valley (LFV), BC. *Atmos. Environ.,* **31,** 2123–2134.

Hooper, W. P., and E. W. Eloranta, 1986: Lidar measurements of wind in the planetary boundary layer: The method, accuracy and results from joint measurements with radiosonde and kytoon. *J. Climate Appl. Meteor.,* **25,** 990–1001.

Matthias, V., and Coauthors, 2004: Vertical aerosol distribution over Europe: Statistical analysis of Raman lidar data from 10 European Aerosol Research Lidar Network (EARLINET) stations. *J. Geophys. Res.,* **109,** D18201, doi:10.1029/2004JD004638.

McIlveen, R., 1992: *Fundamentals of Weather and Climate*. Chapman & Hall, 497 pp.

Melfi, S. H., J. D. Spinhire, S.-H. Chou, and S. P. Palm, 1985: Lidar observation of vertically organized convection in the planetary boundary layer over the ocean. *J. Climate Appl. Meteor.,* **24,** 806–821.

Menut, L., C. Flamant, J. Pelon, and P. H. Flamant, 1999: Urban boundary layer height determination from lidar measurements over the Paris area. *Appl. Opt.,* **38,** 945–954.

Piironen, A. K., and E. Eloranta, 1995: Convective boundary layer mean depths and cloud geometrical properties obtained from volume imaging lidar data. *J. Geophys. Res.,* **100,** 25 569–25 576.

Rampanelli, G., and D. Zardi, 2004: A method to determine the capping inversion of the convective boundary layer. *J. Appl. Meteor.,* **43,** 925–933.

Ruffieux, D., and J. Joss, 2003: Influence of radiation on the temperature sensor mounted on the Swiss radiosonde. *J. Atmos. Oceanic Technol.,* **20,** 1576–1582.

Russell, P. B., E. E. Uthe, F. L. Ludwig, and N. A. Shaw, 1974: A comparison of atmospheric structure as observed with monostatic acoustic sounder and lidar techniques. *J. Geophys. Res.,* **79,** 5555–5566.

Salby, M. L., 1996: *Fundamentals of Atmospheric Physics*. Academic Press, 627 pp.

Sicard, M., C. Pérez, F. Rocadenbosch, J. M. Baldasano, and D. García-Vizcaino, 2006: Mixed layer depth determination in the Barcelona costal area from regular lidar measurements: Methods, results and limitation. *Bound.-Layer Meteor.,* **119,** 135–157.

Siebert, P., F. Beyrich, S. E. Gryning, S. Joffre, A. Rasmussen, and Ph. Tercier, 2001: Review and intercomparison of operational methods for the determination of the mixing height. *Atmos. Environ.,* **34,** 1001–1027.

Steyn, D. G., M. Baldi, and R. M. Hoff, 1998: A new technique to derive mixed layer depth and entrainment zone thickness from lidar profiles. *Extended Abstracts, 19th Int. Laser Radar Conf. (ILRC),* NASA/CP-1988-207671/PT1, Annapolis, MD, NASA GFSC Raman Lidar Group, 461–464.

——, ——, and ——, 1999: The detection of mixed layer depth and entrainment zone thickness from lidar backscatter profiles. *J. Atmos. Oceanic Technol.,* **16,** 953–959.

Stull, R. B., 1988: *An Introduction to Boundary Layer Meteorology*. Kluwer Academic, 666 pp.

Van Pul, W. A. J., A. A. M. Holtslag, and D. P. J. Swart, 1994: A comparison of ABL heights inferred routinely from lidar and radiosondes at noontime. *Bound.-Layer Meteor.,* **68,** 173–191.

Wallace, J. M., and P. V. Hobbs, 1977: *Atmospheric Science—An Introductory Survey*. Academic Press, 467 pp.

Wandinger, U., 2005: Introduction to lidar. *Lidar: Range-Resolved Optical Remote Sensing of the Atmosphere,* C. Weitkamp, Ed., Springer Series of Optical Sciences, Vol. 102, Springer, 1–18.

Wiegner, M., and Coauthors, 2006: Mixing layer height over Munich, Germany: Variability and comparisons of different methodologies. *J. Geophys. Res.,* **111,** D13201, doi:10.1029/2005JD006593.

Zampieri, M., P. Malguzzi, and A. Buzzi, 2005: Sensitivity of quantitative precipitation forecast to boundary layer parameterization: A flash flood case study in the Western Mediterranean. *Nat. Hazards Earth Syst. Sci.,* **5,** 603–612.